




Impact of anisotropy in spin-orbit coupling on the magneto-optical properties of bulk lead halide perovskites

Alyssa Kostadinov-Mutzafi,¹ Jenya Tilchin,¹ Arthur Shapiro ¹ Dmitry N. Dirin,³
Maksym V. Kovalenko,³ Liang Z. Tan ^{2,*} and Efrat Lifshitz ^{1,†}

¹Schulich Faculty of Chemistry, Solid State Institute, Technion – Israel Institute of Technology, Haifa 3200000, Israel

²Molecular Foundry, Lawrence Berkeley National Laboratory, Berkeley, California 94720, USA

³Department of Chemistry and Applied Biosciences, ETH Zürich, 8093 Zurich, Switzerland
and Empa-Swiss Federal Laboratories for Materials Science and Technology, 8600 Zurich, Switzerland



(Received 29 November 2021; revised 20 May 2022; accepted 22 June 2022; published 8 July 2022)

The renaissance of interest in halide perovskites, triggered by their unprecedented performance in optoelectronic applications, elicited worldwide efforts to uncover a variety of intriguing physical properties, with a particular interest in spin-orbit effects. The current work presents the first magneto-optical experimental evidence for anisotropic electron-hole interactions arising from bulk orthorhombic MAPbBr₃. Magneto-photoluminescence spectra, monitored along with several different crystallographic directions, were dominated by dual exciton emission peaks, while each exhibited a highly nonlinear response to a magnetic field. Moreover, these plots depicted asymmetry from $-B_0$ to $+B_0$, with a strong dependence on the axis of observations. A theoretical model implementing anisotropy in the electron-hole interaction, Rashba effect, Landé g factors, and a lesser contribution from an Overhauser effect, corroborated the experimental results. These research discoveries expand the possible applications of excitons in halide perovskites toward optoelectronic and information devices.

DOI: [10.1103/PhysRevB.106.035303](https://doi.org/10.1103/PhysRevB.106.035303)

I. INTRODUCTION

Halide perovskites have been at the forefront of scientific and technological interest for a decade, initiated with the finding of their noteworthy performance in solar cells [1,2], light sources [3,4], X/γ -ray detectors [5,6], and display devices [7–9]. Furthermore, the potential for exploiting spin properties of the halide perovskites for applications in spin-electronic and spin-optical devices has recently emerged [10–14], based on the materials' spin-orbit coupling [15,16], Rashba/Dresselhaus effects [15–19], optically induced spin polarization [17,20,21], and relatively long spin-coherence time compared to classic semiconductors [13,22–25]. Those properties are further elaborated below.

The halide perovskites are interconnected metal halides units, forming a network with octahedral voids filled by organic or inorganic counterions, with a benchmark material bearing the chemical formula AMX_3 (A = counterions [methylammonium, formamidinium, Cs]; M = Pb, Sn; X = I, Cl, Br) [26–29]. The dynamic motion of the loosely bound counterions, the low stiffness of the inorganic network, as well as heterogeneity in dielectric screening endow the halide perovskites with intriguing physical properties such as long diffusion length [30–33], high emission quantum yield [26,34], and tolerance to defects [35–39]. Bulk crystals, as well as a variety of nanoscaled crystals of halide perovskites with different dimensionality, can be feasibly synthesized by

cheap colloidal chemical procedures [9,26,36,40,41] exhibiting a tetragonal or orthorhombic crystallographic structure at ambient and lower temperatures [42]. The electronic band structure of $APbX_3$ is based on the inorganic network, wherein the valence band has a Pb s -orbital character with a minor contribution from a halide p -orbital, while the conduction band has a Pb p -orbital character. The major contribution of a heavy metal to the conduction band results in a spin-orbit coupling, lifting the p -orbital energy degeneracy, thus leaving both the conduction and valence band edges with an angular momentum of $J_e = S_h = 1/2$ (and projection of $S_z = \pm 1/2$). Although band-edge electronic properties are dictated by the inorganic network, the dynamic motion of the A-site ions has a substantial influence on the physical properties of the materials [15,43–45] by inducing a local distortion into the inorganic network, with a plausible breakage of inversion of symmetry [15–17,46–48] and creation of strong anharmonicity [39,43,49–53]. Of note, nonuniform faceting termination at grain boundaries of nanocrystal surfaces (either by PbX_2 or organic chemical groups) induces static polarization and a subsequent inversion symmetry breaking [54–57]. The described dynamic or static distortion, in combination with the poor dielectric screening by the organic moiety, brings about other physical phenomena: the exciton-polaron formation at room temperature [58–61]; strong Fröhlich and anharmonic electron-optical phonon coupling [58,59,62–65]; low coupling to acoustic phonons due to reduced elastic stiffness, slow hot carrier cooling [62,66]; ferroelectricity [64,67–69]; a continual self-healing, and the tolerance to defects [39,70,71].

While isotropic exchange splitting was predicted to always result in an unusual ordering of exciton fine structure

*lztan@lbl.gov

†ssefrat@technion.ac.il

with a triplet-bright state situated below a dark singlet state in methylammonium/Cs-based halide perovskites [55,72], magneto-optical spectroscopy of formamidinium lead bromide (FAPbBr₃) nanocrystals has shown the opposite ordering [112]. The weaker crystal field splitting of FAPbBr₃ compared to CsPbBr₃, or inhomogeneities present in bulk but not nanocrystalline samples, could account for differences between these systems. Anisotropy can potentially reorder and mix these energy levels, depending on its strengths and symmetries. These anisotropies can arise from bulk crystalline anisotropies, noncrystallinities such as grain boundaries, static or dynamic structural distortions arising from interfacial effects, or thermal fluctuations. When inversion symmetric breaking is combined with spin-orbit coupling, Rashba/Dresselhaus effects become active (an explanation on the effect of Rashba/Dresselhaus splitting on the electron-hole interaction can be found in Sec. V in the Supplemental Material (SM) [73]); see also Refs. [24,74–87]. Rashba splitting was observed at zero and higher magnetic fields in a single CsPbBr₃ nanocube [17,88–91], while fast recombination times (<ns) at low temperatures suggest low-lying bright excitons (in contrast to the existence of dark excitons in most common semiconductor quantum dots, such as II-VI, III-V, and IV-VI compounds) [55,92]. Dual recombination emission has been attributed to direct band edges and to the Rashba split indirect transitions [93,94]. Of particular importance is a recent theoretical work which considered the combined contribution of Rashba and Dresselhaus effects on the optical properties [85]. Additionally, spin-coherence studies in APbX₃ have probed carrier dephasing times [21–23,25,95,96], anisotropy in *g*-factor values, and effective masses [97]. These studies have suggested spin decoherence mechanisms such as the Δg mechanism [21], scattering by grain boundaries, inversion symmetry breaking, or by heavy doping [24]. Overall, the discovery of Rashba/Dresselhaus effects in perovskite materials created new horizons to investigate spin properties in these materials and to consider halide perovskites as building blocks in spin-electronic [10,13,89,98] and quantum information devices [23,99,100].

Additionally, the Overhauser effect should be mentioned due to the existence of magnetic neutral abundance isotopes in halide perovskites. The Overhauser effect is initiated when a photogenerated carrier applies a local field on nuclear spins via hyperfine interactions and induces their mutual alignment. The effective magnetic field created by the nuclei (known also as the Overhauser field) reacts on the charge carrier, affecting its polarization and the helicity of a recombination emission. The effective nuclear field may enhance or suppress the Zeeman or Rashba fields [22,101–107]. These spin explorations indicate that spin behavior is a prominent issue in the optical properties of halide perovskite materials; however, they will be dealt here in a minor way, although the topic requires further investigation, particularly exploring the influence of intrinsic anisotropic effects.

The current work reports magneto-photoluminescence measurements of bulk MAPbBr₃ that reveal anisotropic electron-hole interactions. The mentioned effects along with a Zeeman field modify the ordering of the exciton fine-structure and the relaxation processes within it. This is manifested in the magneto-photoluminescence intensities, which revealed turn-

ing points at ± 0.2 Tesla, mainly due to the multicomponent (nonaxial) nature of the electron-hole interaction. Besides these effects, we also discuss a minor contribution from the Overhauser effect detected in magnetic photoluminescence (MPL) and electron spin resonance (ESR) measurements. The following section summarizes the experimental results, supported by a theoretical model and concluding discussion.

II. RESULTS AND DISCUSSION

MAPbBr₃ crystals (typical size of ~ 2 mm) were prepared via a procedure reported previously in the literature [26]. The crystal structures produced and their faceting were characterized by x-ray diffraction, confirming an orthorhombic structure <100 K. The photoluminescence (PL) and magneto-PL (MPL) spectra at low temperatures were obtained by mounting the samples onto a confocal microscope immersed into a liquid He-free cryosystem equipped with an external magnetic field (B_0) operating up to 6 Tesla. For a magnetic resonance measurement, the sample was mounted inside a microwave cavity integrated within the confocal microscope, and a microwave radiation within the cavity was induced through an antenna [17,108,109]. The excitation beam was aligned along the direction of a magnetic field (Faraday configuration) when the sample's crystallographic axis [001] was oriented either parallel or perpendicular to B_0 . A nonresonant excitation beam was focused into a $< 0.5\text{-}\mu\text{m}$ spot via an objective and was scanned across the sample surface, thereby observing different domains. The synthesis and additional experimental details are reported in Appendix A.

Figure 1 depicts representative unpolarized PL spectra, covering the 2.235–2.250-eV spectral window, which were recorded at 4 K. The spectra are associated with emission events from different spots across a single crystal, with orientation of B_0 and the excitation beam (\mathbf{k}) either parallel or perpendicular to the crystal facet [001], as shown by cartoons next to each panel. The spectra in Fig. 1 encompass two emission bands, fitted by the blue and red Gaussians. The narrow bands' FWHM and the small energy shift (~ 8 meV) with respect to the electronic band edge [42] (inset, spot 1) suggest their involvement with excitonic processes. The dual exciton emission peaks have been attributed before to the coexistence of direct and indirect band-edge recombination [93], with the indirect transitions resulting from the presence of an unequal Rashba splitting in the conduction and valence bands [16,17,42,54]. Alternatively, dual emission may be related to a free and bound (or charged) exciton emission processes.

It is important to note that examination of a wider spectral range occasionally exposed an asymmetric tail as well as an additional band ~ 40 meV below the exciton region. An illustrative case is shown in the inset of spot 4 in Fig. 1, and other results are available in the SM, Fig. S1 [73]. The asymmetric tail is compatible with longitudinal optical replica [59,93,110], while the wide band at low energies may be related to a self-trap recombination [111–113]. The intensity of the deep luminescence is strongly dependent on the spot of observation and angle with respect to crystal symmetry axis (not shown here). The mentioned nonexcitonic recombination processes are not elaborated any further.

Further on, the PL spectra of spots 1–4 were recorded under the presence of an external magnetic field (B_0) from

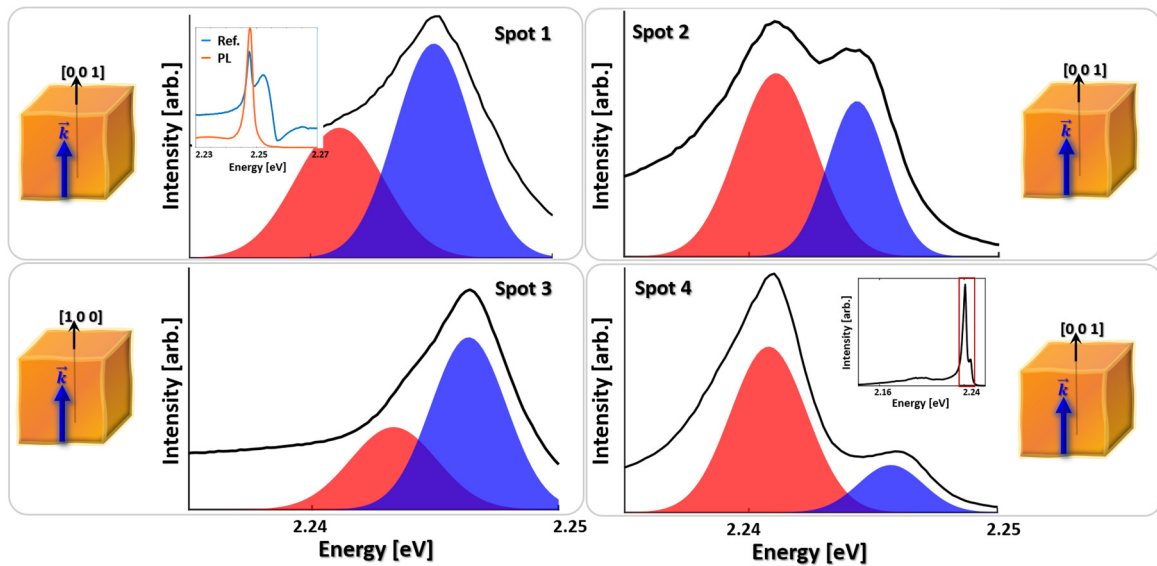


FIG. 1. Photoluminescence (PL) spectra of a few different spots on the sample surface, all fitted by two Gaussian curves (blue and red). The spectra were recorded at 4 K and $B_0 = 0$ Tesla, with optical alignment as given by cartoons at the margins. (Insets) Spot 1: PL and reflection spectra around the exciton spectral region. Spot 4: A PL spectrum of a wide spectral range.

zero to ± 6.0 Tesla [referred hereon as $MPL(B_0)$ curves]. Plots of the PL integrated intensity of the red or blue components of the mentioned spots versus the strength of B_0 between ± 2.0 Tesla are shown in Figs. 2(a)–2(d). Those $MPL(B_0)$

curves possess a nonlinear dependence on B_0 , encompassing rich information that will be thoroughly elaborated in the following discussion. Similar plots complementing the $MPL(B_0)$ dependence > 2.0 Tesla are given in the SM, Fig. S2 [73],

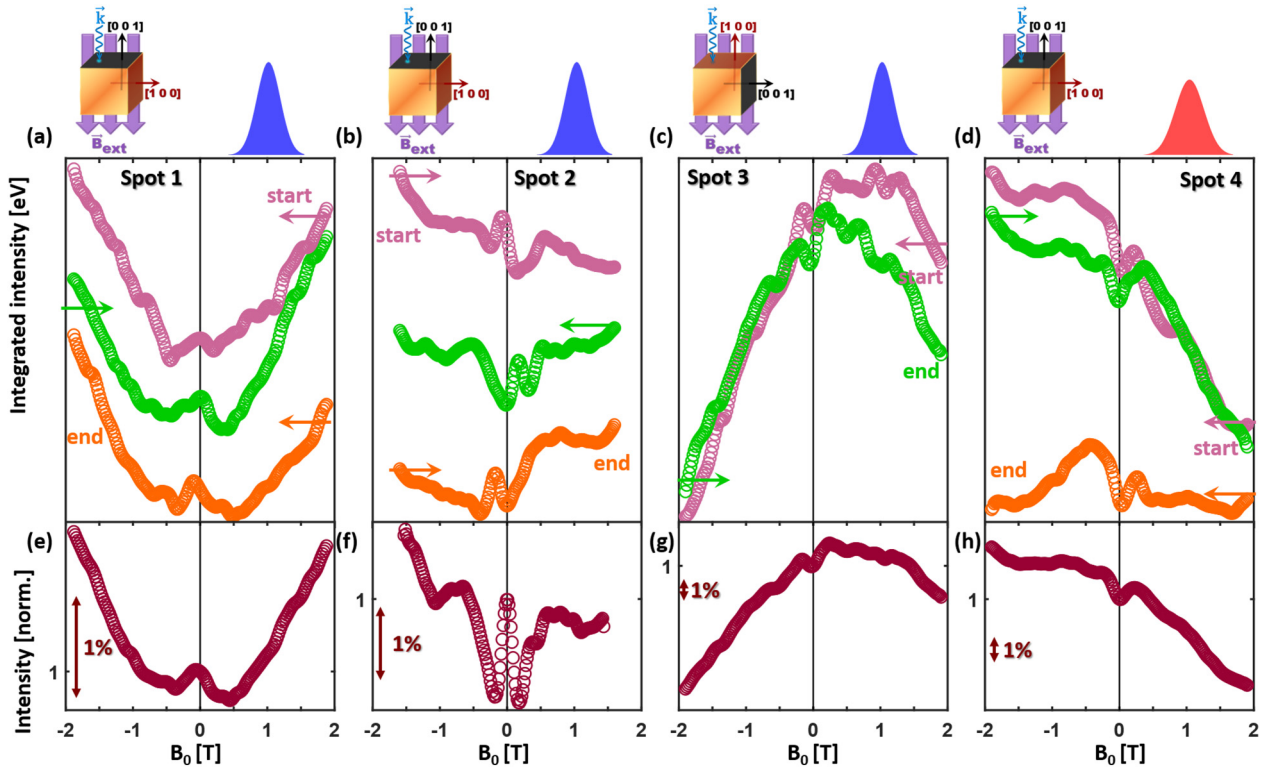


FIG. 2. Magneto-PL plots vs strength of an external magnetic field (B_0). (a) to (d) are the $MPL(B_0)$ curves of spots 1 to 4 in Fig. 1, respectively. Cartoons above illustrate the excitation and magnetic field orientation with respect to the [001] crystal plane. The Gaussian curves refer to the detected spectral regimes. The top panels display the integrated intensity of the PL band collected upon a scan of the magnetic field from the negative to the positive side or vice versa (see colored arrows). The bottom panels (e–h) illustrate averaging traces of $MPL(B_0)$ curves above them.

revealing a Zeeman behavior at the high field limit, in agreement with observations found in a single CsPbBr₃ nanocube [17].

The panels in Fig. 2 display a few scans from negative (positive) to positive (negative) magnetic field values (see directing arrows). These plots show qualitatively reproducible features around $B_0 = 0$ Tesla; however, their relative intensities attenuate according to the direction of the scan. To emphasize the meaningful features, a mean plot for each spot is displayed in Figs. 2(e)–2(h), where the intensity at $B_0 = 0$ Tesla was normalized to a value of 1. For the purpose of the coming theoretical simulation, the central MPL peaks in Fig. 2(b) were aligned to the $B_0 = 0$ Tesla point, and their averaging is illustrated in Fig. 2(f).

The MPL(B_0) plots of spots 1 and 2 are associated with two different locations on the sample surface, monitored at the same alignment of $\mathbf{B}_0 \parallel \mathbf{k} \parallel [001]$. These plots exhibit a few similar phenomena, including dominating negative extrema at ± 0.2 or ± 0.4 Tesla and additional weak ones at ± 1.2 Tesla, being particularly pronounced at spot 2. The intensity changes are about 1% compared to the value at $B_0 = 0$ Tesla (see scale bars).

Beyond the extreme points, the MPL intensity deflects toward positive values and gradually increases up to ± 2.0 Tesla in a nonlinear fashion. The scans in Figs. 2(a) and 2(b) also show an asymmetric evolution when comparing the negative and positive field branches, accompanied by a shift of a central feature at $B_0 = 0$ Tesla (mainly in spot 2), together suggesting the occurrence of stray magnetic fields, probable originating from an Overhauser effect. To probe a possible stray magnetization, we perform a control experiment utilizing ESR spectroscopy, Fig. S4 [73], in which irradiation created ESR features which surprisingly remained unchanged for a couple of hours after turning off the exposure to light. The result implies that a photogenerated carrier may have been trapped at a defect site [114], while its prolonged decay time is associated with a coupling to nuclear spins (the so-called Overhauser effect).

Figure 2(c) displays the MPL(B_0) plot of spot 3, which was monitored with an alignment of $\mathbf{B}_0 \parallel \mathbf{k} \perp [001]$, i.e., on a different facet than spots 1, 2, and 4. MPL(B_0) of spot 3 exhibits positive extrema surrounding $B_0 = 0$ Tesla and centering at ± 0.2 Tesla. At stronger fields, MPL(B_0) decreases in a nonlinear fashion. This is in contrast to the typical behavior seen in spots 1 and 2. Additionally, there is strong asymmetry between the negative and positive magnetic field branches. The pronounced asymmetry is correlated with the lack of a mirror plane normal to the direction of \mathbf{B}_0 , as discussed below. Representative circularly polarized PL spectra of spots 2 and 3 and their degree of circular polarization (DCP) versus magnetic field strength are depicted in Fig. S3 [73]. Overall, the DCP observations reveal obvious asymmetry at higher magnetic fields for spot 3, consistent with the behavior seen in Fig. 2(c).

Figure 2(d) illustrates MPL(B_0) plots of the red PL band of spot 4, with alignment of $\mathbf{B}_0 \parallel \mathbf{k} \parallel [001]$. This plot substantially deviates from that of spots 1 and 2, possessing a strong asymmetry between positive and negative \mathbf{B}_0 directions, as well as having extrema away from $B_0 = 0$ Tesla, diverging in their intensity depending on the scanning direction. These features

could be due to recombination either at a misaligned grain or a new recombination feature, like shallow trap-to-band or a trion emission [22,42,115,116]. The observation here can be correlated with previous transient PL decays measured on the same samples examined in this study, which exposed double components, one with a typical lifetime $< \text{ns}$ associated with the neutral exciton emission and a second one with a lifetime of ~ 12 ns, presumably related to a lower-energy component (the red band in Fig. 1) [42]. We note that a recent publication uncovered a long lifetime of a trion beyond that of a neutral exciton [117].

In the following theoretical section, we solely focus on the reproducible MPL(B_0) features (Fig. 2), namely, the turning points at low magnetic fields $B_0 < 1$ Tesla, and the opposite trends of spots 1,2 compared to spot 3, focusing on the blue PL band. It will be shown that these are the consequences of anisotropic electron-hole interactions and anisotropic g factors.

III. THEORETICAL SIMULATION AND DISCUSSION

The low-lying excitonic levels are made up of electron-hole pairs of $S = 1/2$ valence bands, ($|\uparrow_h\rangle, |\downarrow_h\rangle$), and $J = 1/2$ conduction bands, ($|\uparrow_e\rangle, |\downarrow_e\rangle$). In the lowest approximation, the excitonic levels are fourfold degenerate at zero magnetic field:

$$|\Psi_{0,0}\rangle = \frac{1}{\sqrt{2}}(|\downarrow_e\uparrow_h\rangle - |\uparrow_e\downarrow_h\rangle), \quad (1a)$$

$$|\Psi_{1,0}\rangle = \frac{1}{\sqrt{2}}(|\downarrow_e\uparrow_h\rangle + |\uparrow_e\downarrow_h\rangle), \quad (1b)$$

$$|\Psi_{1,1}\rangle = |\uparrow_e\uparrow_h\rangle, \quad (1c)$$

$$|\Psi_{1,-1}\rangle = |\downarrow_e\downarrow_h\rangle. \quad (1d)$$

The triplets $|\Psi_{1,m}\rangle$ [Eqs. (1c)–(1d)] are bright emitting states, while the singlet $|\Psi_{0,0}\rangle$ [Eq. (1a)] is a dark state [55]. In the high- B_0 -field limit, the excitonic levels are split by the Zeeman field and are separated into the levels $|\downarrow_e\uparrow_h\rangle, |\uparrow_e\downarrow_h\rangle, |\uparrow_e\uparrow_h\rangle, |\downarrow_e\downarrow_h\rangle$ [Fig. 3(a), dashed black lines].

Anisotropic electron-hole interactions lift the degeneracy at $B_0 = 0$ Tesla and change the character of excitonic states in the low- B_0 -field limit. We include these effects and an additional Zeeman effect in the Hamiltonian:

$$H = \vec{\sigma}_e \cdot \vec{V} \cdot \vec{\sigma}_h + \frac{1}{2}g_e\mu_B\vec{B} \cdot \vec{\sigma}_e + \frac{1}{2}g_h\mu_B\vec{B} \cdot \vec{\sigma}_h. \quad (2)$$

Here \vec{V} is a real 3×3 matrix representing an effective electron-hole interaction, which includes anisotropy [55], and \vec{B} is the total magnetic field, which is dominated by the applied field \vec{B}_0 , besides having a small Overhauser component.

At the measured temperatures, MAPbBr₃ has a centrosymmetric crystal structure. However, bulk noncrystallinities such as grain boundaries and local strains break inversion symmetry, leading to MPL(B_0) dependence on the detected spot and its faceting. In Eq. (2), the term $\vec{\sigma}_e \cdot \vec{V} \cdot \vec{\sigma}_h$ is a generic electron-hole interaction that preserves time-reversal symmetry while allowing for anisotropy [118]. Contributions from the isotropic parts of the exchange interaction, and the isotropic part of Rashba/Dresselhaus effects [55], determine the identity part of $\vec{V} \propto \mathbf{I}$ (\mathbf{I} being the unit matrix). As the

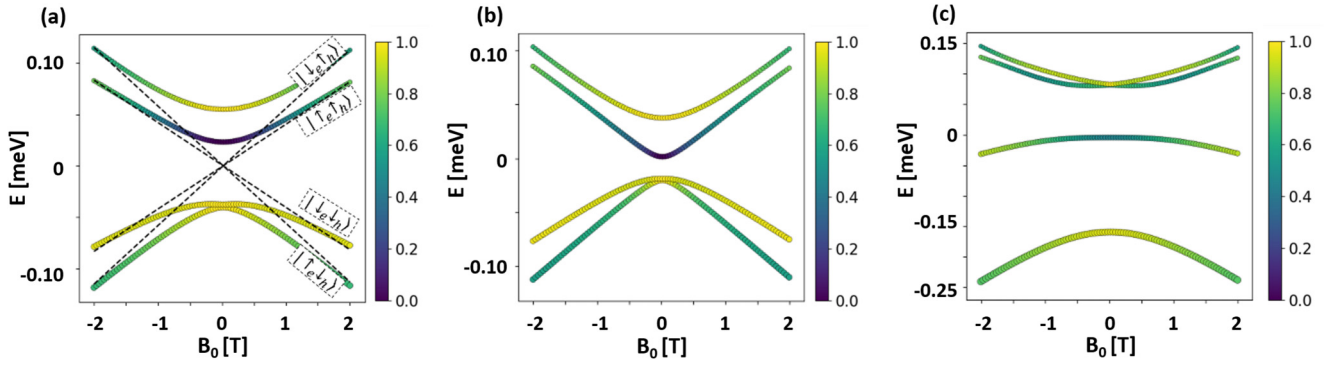


FIG. 3. (a)–(c) Exciton energy-level diagrams under the influence of anisotropic electron-hole interactions and the Zeeman effects, corresponding to the high-energy exciton along the following directions: (a) $k \parallel \mathbf{B}_0 \parallel [001]$ in spot 1; (b) $k \parallel \mathbf{B}_0 \parallel [001]$ in spot 2; (c) $k \parallel \mathbf{B}_0 \perp [001]$ in spot 3. The transition dipole intensities are designated according to the color scale, and the population of each excitonic state is represented by the marker size. Annotations of the exciton wave functions in a high-field limit are shown in (a). Exciton energy levels without spin-orbit couplings are depicted by the black dashed lines in (a).

magnetic field is increased from the low-field limit (where Zeeman effect is small) to high-field limit (where the Zeeman effect is more important), both the transition dipoles and excitonic level energy splitting change. The evolution of the excitonic populations and consequently, the MPL integrated intensity, is a result of the crossover between low and high Zeeman limits. In the following, we discuss the consequences of these effects on the energy-level population and on the MPL of excitonic states. Excitonic populations are obtained from a quantum master equation approach (details in Appendix B).

Figure 4(a) shows the measured MPL(B_0) curve and the theoretical fit for spot 1, the case with $k \parallel \mathbf{B} \parallel [001]$. There are small dips in that MPL(B_0) plot at low magnetic fields, followed by an increase in PL intensity at higher fields. To explain these features, we find that it is sufficient to use a simplified model where

$$\vec{\sigma}_e \cdot \vec{V} \cdot \vec{\sigma}_h = V_a \sigma_a^{(e)} \sigma_a^{(h)} + V_b \sigma_b^{(e)} \sigma_b^{(h)} + V_c \sigma_c^{(e)} \sigma_c^{(h)}, \quad (3)$$

which has a major axis (a) for the electron-hole coupling, and two minor (orthogonal) components (b, c). For spot 1, we find that $V_a = -38.9 \mu\text{eV}$, $V_b = 7.22 \mu\text{eV}$, $V_c = 8.64 \mu\text{eV}$, with the major axis tilted at 72.8° relative to the magnetic field. This multicomponent nature of the coupling with three separate axes of interaction is important to explain the MPL dips at low magnetic fields. In the SM, Fig. S5 [73], we show that a model with only the major electron-hole component is unable to explain these features. Furthermore, the depths of the dips are dependent on the angle between the major component and the magnetic field axis. Taken together, these observations provide support for the influence of anisotropic structure in the bulk of the material, which produces an electron-hole coupling primarily oriented along a single axis, and with some secondary components.

We predict strong reordering and intermixing of singlet and triplet energy levels from these electron-hole couplings. As a result, transition dipoles change with magnetic fields (Fig. 3). At these magnetic fields, all four levels have

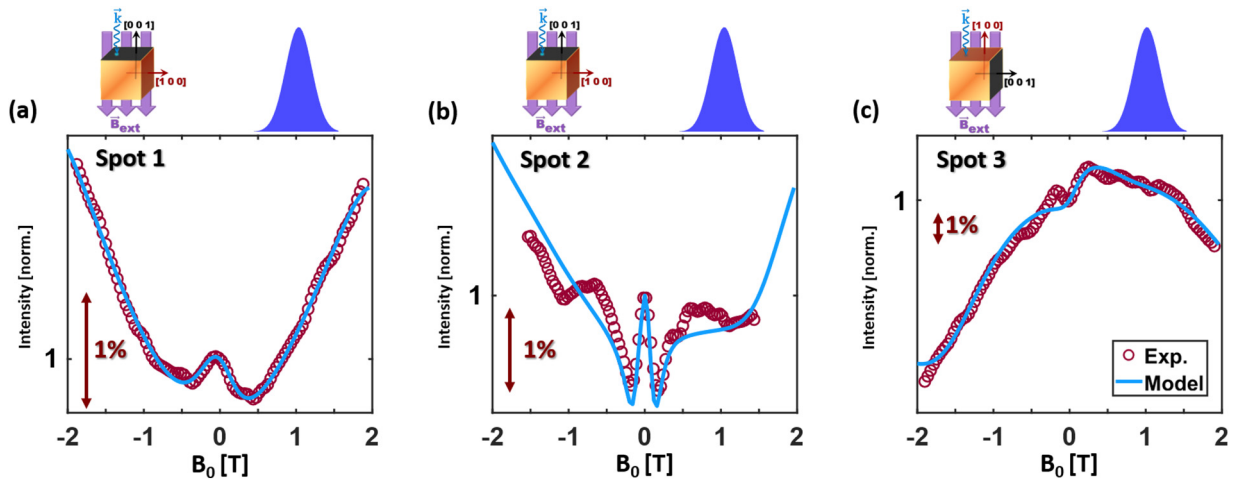


FIG. 4. A Comparison between the MPL experimental data, obtained along different crystal orientations, with the anisotropic electron-hole interaction QME model: (a) $k \parallel \mathbf{B}_0 \parallel [001]$, high-energy exciton in spot 1; (b) $k \parallel \mathbf{B}_0 \parallel [001]$, high-energy exciton in spot 2; and (c) $k \parallel \mathbf{B}_0 \perp [001]$, high-energy exciton in spot 3.

significant population because the level splitting is the same order of magnitude as the thermal energy scale, and also because of the effect of optical pumping.

A similar overall trend is seen on spot 2, $\mathbf{k} \parallel \|\mathbf{B}_0\|$ [001] [Fig. 4(b)]. We obtain electron-hole coupling components $V_a = -19.6 \mu\text{eV}$, $V_b = 8.69 \mu\text{eV}$, and $V_c = 9.35 \mu\text{eV}$, with the major axis tilted at 73.6° relative to the magnetic field. These parameters are similar to those for spot 1 and similarly describe the MPL(B_0) dips at low magnetic field as well as the overall increasing MPL trend, which is expected since both spots are on the same facet. However, the experimental MPL of spot 2 contains additional shoulders at $B_0 = 1.5$ Tesla. It is possible that they are an additional contribution from multiple grain boundaries in the same spot area, which are not captured by this model, that treats only a single four-band manifold of states.

The opposite MPL trend of spot 3 [Fig. 4(c)] compared to spots 1 and 2 is explained by g -factor anisotropy. We use the electron and hole g factors as fitting parameters in the quantum master equation (QME) model for these spots and find that the values of g_e and g_h fitted to the QME model are similar for spot 1 ($g_e = 1.555$, $g_h = -0.270$) and spot 2 ($g_e = 1.589$, $g_h = -0.2017$), and different for spot 3 ($g_e = 1.931$, $g_h = -0.7278$), see Sec. IV, Table I in the SM [73]. Due to crystalline anisotropy, we expect different g factors when the magnetic field is parallel or normal to [001] [88,97,119]. Consistent with previous literature [97,119], we find that g_e and g_h have different signs, with g_e being of larger magnitude. In Sec. IV A in the SM [73], we show that the effect of the g factors on the MPL trends is rather general and independent of the exact values of the electron-hole couplings used in the model; as the magnitudes of $|g_e|$ and $|g_h|$ are increased, the MPL(B_0) curves switch from a trend of increasing with B_0 to decreasing with B_0 . The g factors affect the MPL(B_0) trends by controlling the excitonic populations through the excitonic level splitting.

In the case of $\mathbf{k} \parallel \mathbf{B}_0 \perp$ [001] [spot 3, Fig. 4(c)], we find an asymmetric dependence of PL at positive and negative fields, unlike the other orientations. The introduction of the incoherent processes of recombination and thermal relaxation (details in Appendix B) breaks the time-reversal symmetry of the system. Therefore, under a change in direction of magnetic field from $+\mathbf{B}_0$ to $-\mathbf{B}_0$, the MPL(B_0) curve exposes a deviation from a perfect symmetry. Nevertheless, there are features which appear approximately symmetrically on $+\mathbf{B}_0$ and $-\mathbf{B}_0$ wings of the MPL(B_0) curves, such as the dips and shoulders in Figs. 4(a) and 4(b). The symmetrical features are associated with exciton levels or transition dipoles, occurring at $+\mathbf{B}_0$ as well as at $-\mathbf{B}_0$. The asymmetrical features, such as the unequal magnitudes of the dips at $+\mathbf{B}_0$ and $-\mathbf{B}_0$, can be rationalized as arising from different excitonic populations at $+\mathbf{B}_0$ and $-\mathbf{B}_0$. In our simulations, we predict population asymmetries of less than 1% between $+\mathbf{B}_0$ and $-\mathbf{B}_0$. While small, these asymmetries are nonetheless observable in the measured PL spectra. The observation of asymmetry in $+\mathbf{B}_0$ and $-\mathbf{B}_0$ is evidence for the lack of a mirror plane normal to \mathbf{B}_0 . The lack of this mirror plane results from non-crystallinities such as grain boundaries, even if the perfectly

crystalline lattice does have mirror symmetry. In order to fit the large asymmetry of spot 3, we use the general form of the electron-hole coupling \vec{V} instead of the simplified form in Eq. (3). The magnitudes of the fitted electron-hole couplings are also larger on this facet (see Sec. IV, Table I, in the SM [73]).

In general, anisotropic electron-hole interactions cause intermixing between singlet and triplet states, resulting in four excitonic levels each with some oscillator strength. The nature of this intermixing depends on the symmetries of the electron-hole interaction. On spots 1 and 2, the interaction has approximate axial symmetry, as shown above. The singlet $|\Psi_{0,0}\rangle$ and triplet states $|\Psi_{1,m}\rangle$ are therefore eigenvectors at zero magnetic field and show up as dark and bright states in the transition dipole diagram [Figs. 3(a) and 3(b)]. On spot 3, however, the electron-hole interaction is not as strongly dominated by a single contribution, and intermixing between singlet and triplet occurs even at zero magnetic field. These results suggest that, besides crystalline anisotropic contributions which would be present in the bulk, there are also facet-dependent anisotropic contributions, possibly arising from Rashba effects (Sec. V in the SM [73]).

In these bulk samples, the crossover between low and high Zeeman limits typically occur in the range of $B_0 < 0.5$ Tesla, as seen in Fig. 3, where the changes in color signify changes in transition dipoles and hence the excitonic character between these limits. In comparison, halide perovskite nanocrystals have a larger crossover magnetic field of $B_0 = 2.0$ Tesla [17]. This is likely due to strong Rashba effects being present at the surfaces of nanocrystals, which have a significant surface area to volume ratio.

The hysteresis and the shifts of the central MPL features in Fig. 2 can be understood as arising from nuclear magnetic fields. To estimate the magnitude of the Overhauser effect in our system, we compute excitonic spin polarizations as predicted by the QME model, $\langle \vec{S} \rangle = \text{Tr}[(\vec{S}_e + \vec{S}_h)\rho]$, where \vec{S}_e and \vec{S}_h are the electron and hole spin operators. Because unpolarized light has been used, excitonic spin polarizations arise not from absorption of circularly polarized photons but from separation of the excitonic energy levels. Following [22], we solve nuclear spin polarization and Overhauser fields induced by hyperfine coupling of the electronic and nuclear spin systems. The Overhauser field is $\vec{B}_N = A \vec{I}_N / (g\mu_B)$, where the nuclear spin polarization \vec{I}_N at steady state is given by $\frac{d}{dt}\vec{I}_N = \frac{\langle \vec{S} \rangle}{T_{hf}} - \frac{\vec{I}_N}{T_N} = 0$ [120], with T_{hf} and T_N being the hyperfine interaction time and nuclear spin relaxation times, respectively. We use a hyperfine coupling of $A = 20 \mu\text{eV}$ from ^{207}Pb at natural abundance [22]. We find that Overhauser fields are small compared to the external magnetic fields, ranging from $B_N \approx -0.02 B_0$ at $\frac{T_{hf}}{T_N} \approx 1$, to $B_N \approx -0.10 B_0$ at $\frac{T_{hf}}{T_N} \approx 5$.

The direction of the Overhauser field is opposite to the external magnetic field. This explains the hysteretic behavior that is observed in the magneto-PL data. When the direction of the magnetic field sweep is reversed, the magneto-PL features are consistently shifted so that they appear at more negative fields when doing a negative-to-positive sweep after a positive-to-negative one, and at more positive fields

when doing the opposite. This behavior is present in all spots and is especially apparent in the movement of the central peak in spot 2, as a result of the persistence of the Overhauser field over the course of the measurements. The Overhauser field opposes the external field and tends to lag behind the changes in the external field. In our fitting to the QME model, we separate these nuclear spin hysteretic effects from the purely excitonic effects by taking an average of positive-to-negative and negative-to-positive sweeps, shifting the magneto-PL data so that the central peak occurs at $B_0 = 0$ Tesla.

IV. CONCLUSIONS

In conclusion, we have shown that anisotropic electron-hole interactions are present in the bulk of halide perovskites, via magneto-optical spectroscopy and quantum master equation modeling. Even though these anisotropies vary from location to location, they show reproducible features in the $MPL(B_0)$ plots at low magnetic fields and facet-dependent MPL trends at high magnetic fields. We show that these are consequences of a multicomponent electron-hole coupling and g -factor anisotropy. Besides bulk crystalline anisotropy, a possible contributor to these anisotropic couplings is the Rashba effect, which is facet dependent and affected by different nanocrystallinities within the bulk of halide perovskites, such as grain boundaries. These results show that symmetry breaking in halide perovskites have measurable consequences on the excitonic level structure of these materials, which must be considered during the materials engineering process.

ACKNOWLEDGMENTS

The authors express their gratitude to Professor Alexander Efros for the useful scientific discussion and constructive comments regarding the manuscript. L.Z.T. was supported by the Molecular Foundry, a DOE Office of Science User Facility supported by the Office of Science, Office of Basic Energy Sciences, of the U.S. Department of Energy under Contract No. DE-AC02-05CH11231. This research used resources of the National Energy Research Scientific Computing Center, a DOE Office of Science User Facility supported by the Office of Science of the U.S. Department of Energy under Contract No. DE-AC02-05CH11231. E.L. and A.K.M. express their thanks for the financial support by the European Commission via the Marie Skłodowska-Curie action Phonsi (H2020-MSCA-ITN-642656), the Israel Science Foundation (No. 2528/19), and the joint USA National Science Foundation–USA/Israel Binational Science Foundation (NSF-BSF, No. 2017637). The work at ETH Zurich (D.N.D. and M.V.K.) was financially supported by the Swiss National Science Foundation (Grant Agreement No. 186406).

APPENDIX A: SYNTHESIS AND EXPERIMENTAL SETUP

The bulk single crystal of $MAPbBr_3$ with dimensions of $3 \times 3 \times 2$ mm was prepared using a procedure described in Ref. [42]. The PL and MPL spectra of the crystal were recorded using a fiber-based confocal microscope with $NA = 0.65$. The spatial resolution of the excitation was $\sim 0.5 \mu\text{m}$,

and immersion took place in a cryogenic system. All the measurements were performed in a temperature range from 4.0 to 4.5 K. The sample was excited with a 405-nm CW laser diode. The PL and MPL signals were recorded with an electrically cooled EM CCD camera (Andor, NewtonTM EM CCD) with spectral resolution of the detection system of $\sim 300 \mu\text{eV}$.

APPENDIX B: QUANTUM MASTER EQUATION SIMULATION

We perform modeling of excitonic populations using a quantum master equation approach. Exciton populations are determined by the balance between optical pumping into bright excitonic levels, incoherent relaxation into low-energy excitonic levels, and radiative recombination. The evolution of the density matrix ρ of these excitonic levels is given by the QME [97]:

$$\frac{d\rho}{dt} = -\frac{i}{\hbar}[\mathbf{H}, \rho] + \left(\frac{d\rho}{dt}\right)_F + \left(\frac{d\rho}{dt}\right)_R + \left(\frac{d\rho}{dt}\right)_T. \quad (\text{B1})$$

The terms $\left(\frac{d\rho}{dt}\right)_F$, $\left(\frac{d\rho}{dt}\right)_R$, and $\left(\frac{d\rho}{dt}\right)_T$ represent optical pumping, radiative recombination, and thermal relaxation of the excitonic levels, which add, remove, and redistribute, respectively, the population among the four excitonic states. We solve Eq. (B1) for steady-state excitonic populations as a function of magnetic field, finding \vec{V} values which explain the experimental $MPL(B_0)$.

In our model, the optical pumping term is given by $\left(\frac{d\rho_{ii}}{dt}\right)_F = F_i$, with F_i describing the rate of pumping into state i . In our case of nonresonant optical pumping (405 nm), excitonic population results from carrier relaxation from higher-energy states instead of direct optical pumping, and we approximate F_i to be a constant over the four excitonic levels. Radiative recombination is given by $\left(\frac{d\rho_{ii}}{dt}\right)_R = \tau^{-1}\rho_{ii}$, for i being to one of the three bright triplets $\Psi_{1,1}$, $\Psi_{1,0}$, and $\Psi_{1,-1}$. Thermal relaxation among the excitonic levels is given by $\left(\frac{d\rho_{aa}}{dt}\right)_T = \sum_b (k_{ab}\rho_{bb} - k_{ba}\rho_{aa})$, with the rate constants $k_{ab} = \tau_{ph}^{-1} e^{\beta E_a} / \sum_c e^{\beta E_c}$ representing the population relaxation rate between the excitonic eigenstates a and b , chosen so that a Boltzmann distribution is achieved in the absence of optical pumping and recombination effects. The magneto-PL is obtained by computing $\text{Tr}[\Lambda\rho]$, where Λ_{ii} are nonzero solely for the bright states under a given detector configuration (considering the $J = 1/2$ and $S = 1/2$ conduction and valence bands only). Here we detect unpolarized PL along the same axis as the optical pump; that is, Λ_{ii} is nonzero only for the bright triplets $\Psi_{1,1}$ and $\Psi_{1,-1}$.

In these simulations we fix the simulation temperature at the experimental value of 4 K, the recombination time constant at $\tau = 200$ ps, and the thermalization time constant at $\tau_{ph} = 20$ fs. The elements of the electron-hole coupling \vec{V} and the g factors are taken as fitting parameters.

- [1] M. M. Lee, J. Teuscher, T. Miyasaka, T. N. Murakami, and H. J. Snaith, Efficient hybrid solar cells based on meso-superstructured organometal halide perovskites, *Science* **338**, 643 (2012).
- [2] L. Etgar, P. Gao, Z. Xue, Q. Peng, A. K. Chandiran, B. Liu, M. K. Nazeeruddin, and M. Grätzel, Mesoscopic $\text{CH}_3\text{NH}_3\text{PbI}_3/\text{TiO}_3$ heterojunction solar cells, *J. Am. Chem. Soc.* **134**, 17396 (2012).
- [3] Q. A. Akkerman, G. Rainò, M. V. Kovalenko, and L. Manna, Genesis, challenges and opportunities for colloidal lead halide perovskite nanocrystals, *Nat. Mater.* **17**, 394 (2018).
- [4] S. Yakunin, L. Protesescu, F. Krieg, M. I. Bodnarchuk, G. Nedelcu, M. Humer, G. De Luca, M. Fiebig, W. Heiss, and M. V. Kovalenko, Low-Threshold amplified spontaneous emission and lasing from colloidal nanocrystals of caesium lead halide perovskites, *Nat. Commun.* **6**, 8056 (2015).
- [5] S. Yakunin, D. N. Dirin, Y. Shynkarenko, V. Morad, I. Cherniukh, O. Nazarenko, D. Kreil, T. Nauser, and M. V. Kovalenko, Detection of gamma photons using solution-grown single crystals of hybrid lead halide perovskites, *Nat. Photon.* **10**, 585 (2016).
- [6] H. Deng, X. K. Yang, D. D. Dong, B. Li, D. Yang, S. J. Yuan, K. K. Qiao, Y. B. Cheng, J. Tang, and H. S. Song, Flexible and semitransparent organolead triiodide perovskite network photodetector arrays with high stability, *Nano Lett.* **15**, 7963 (2015).
- [7] X. Zhang, H. Lin, H. Huang, C. Reckmeier, Y. Zhang, W. C. H. Choy, and A. L. Rogach, Enhancing the brightness of cesium lead halide perovskite nanocrystal based green light-emitting devices through the interface engineering with perfluorinated ionomer, *Nano Lett.* **16**, 1415 (2016).
- [8] H. Deng, D. D. Dong, K. K. Qiao, L. L. Bu, B. Li, D. Yang, H. E. Wang, Y. B. Cheng, Z. X. Zhao, J. Tanga, and H. S. Song, Growth, patterning and alignment of organolead iodide perovskite nanowires for optoelectronic devices, *Nanoscale* **7**, 4163 (2015).
- [9] M. Y. Leng, Z. W. Chen, Y. Yang, Z. Li, K. Zeng, K. H. Li, G. D. Niu, Y. S. He, Q. C. Zhou, and J. Tang, Lead-Free, blue emitting bismuth halide perovskite quantum dots, *Angew. Chemie-International Ed.* **55**, 15012 (2016).
- [10] D. Sun, C. Zhang, M. Kavand, K. J. van Schooten, H. Malissa, M. Groesbeck, R. McLaughlin, C. Boehme, and Z. V. Vardeny, Spintronics of organometal trihalide perovskites, [arXiv:1608.00993](https://arxiv.org/abs/1608.00993).
- [11] J. Wang, X. Pan, C. Zhang, H. Guo, and Z. V. Vardeny, Light-controlled spintronic device based on hybrid organic-inorganic perovskites, *J. Photon. Energy* **8**, 032207 (2018).
- [12] A. Pandey, S. Brovelli, R. Viswanatha, L. Li, J. M. Pietryga, V. I. Klimov, and S. A. Crooker, Long-lived photoinduced magnetization in copper-doped ZnSe-CdSe core-shell nanocrystals, *Nat. Nanotechnol.* **7**, 792 (2012).
- [13] J. Wang, C. Zhang, H. Liu, R. McLaughlin, Y. Zhai, S. R. Vardeny, X. Liu, S. McGill, D. Semenov, H. Guo, R. Tsuchikawa, V. V. Deshpande, D. Sun, and Z. V. Vardeny, Spin-optoelectronic devices based on hybrid organic-inorganic trihalide perovskites, *Nat. Commun.* **10**, 129 (2019).
- [14] L. Leppert, S. E. Reyes-Lillo, and J. B. Neaton, Electric field- and strain-induced Rashba effect in hybrid halide perovskites, *J. Phys. Chem. Lett.* **7**, 3683 (2016).
- [15] F. Zheng, L. Z. Tan, S. Liu, and A. M. Rappe, Rashba spin-orbit coupling enhanced carrier lifetime in $\text{CH}_3\text{NH}_3\text{PbI}_3$, *Nano Lett.* **15**, 7794 (2015).
- [16] M. Kepenekian, R. Robles, C. Katan, D. Saporì, L. Pedesseau, and J. Even, Rashba and Dresselhaus effects in hybrid organic-inorganic perovskites: From basics to devices, *ACS Nano* **9**, 11557 (2015).
- [17] M. Isarov, L. Z. Tan, M. I. Bodnarchuk, M. V. Kovalenko, A. M. Rappe, and E. Lifshitz, Rashba effect in a single colloidal CsPbBr_3 perovskite nanocrystal detected by magneto-optical measurements, *Nano Lett.* **17**, 5020 (2017).
- [18] M. Kepenekian and J. Even, Rashba and Dresselhaus couplings in halide perovskites: Accomplishments and opportunities for spintronics and spin-orbitronics, *J. Phys. Chem. Lett.* **8**, 3362 (2017).
- [19] F. Wang, H. Gao, C. de Graaf, J. M. Poblet, B. J. Campbell, and A. Stroppa, Switchable Rashba anisotropy in layered hybrid organic-inorganic perovskite by hybrid improper ferroelectricity, *npj Comput. Mater.* **6**, 183 (2020).
- [20] Y. S. Park, S. Guo, N. S. Makarov, and V. I. Klimov, Room temperature single-photon emission from individual perovskite quantum dots, *ACS Nano* **9**, 10386 (2015).
- [21] C. Zhang, D. Sun, C. X. Sheng, Y. X. Zhai, K. Mielczarek, A. Zakhidov, and Z. V. Vardeny, Magnetic field effects in hybrid perovskite devices, *Nat. Phys.* **11**, 427 (2015).
- [22] V. V. Belykh, D. R. Yakovlev, M. M. Glazov, P. S. Grigoryev, M. Hussain, J. Rautert, D. N. Dirin, M. V. Kovalenko, and M. Bayer, Coherent spin dynamics of electrons and holes in CsPbBr_3 perovskite crystals, *Nat. Commun.* **10**, 673 (2019).
- [23] P. Odenthal, W. Talmadge, N. Gundlach, R. Wang, C. Zhang, D. Sun, Z. G. Yu, Z. Valy Vardeny, and Y. S. Li, Spin-Polarized exciton quantum beating in hybrid organic-inorganic perovskites, *Nat. Phys.* **13**, 894 (2017).
- [24] D. Giovanni, H. Ma, J. Chua, M. Grätzel, R. Ramesh, S. Mhaisalkar, N. Mathews, T. C. Sum, M. Grätzel, R. Ramesh, S. Mhaisalkar, N. Mathews, T. C. Sum, M. Grätzel, R. Ramesh, S. Mhaisalkar, N. Mathews, T. C. Sum, M. Grätzel, R. Ramesh, S. Mhaisalkar, N. Mathews, T. C. Sum, M. Grätzel, R. Ramesh, S. Mhaisalkar, N. Mathews, and T. C. Sum, Highly spin-polarized carrier dynamics and ultralarge photoinduced magnetization in $\text{CH}_3\text{NH}_3\text{PbI}_3$ perovskite thin films, *Nano Lett.* **15**, 1553 (2015).
- [25] H. Utzat, W. Sun, A. E. K. Kaplan, F. Krieg, M. Ginterseder, B. Spokoiny, N. D. Klein, K. E. Shulenberger, C. F. Perkinson, M. V. Kovalenko, and M. G. Bawendi, Coherent single-photon emission from colloidal lead halide perovskite quantum dots, *Science* **363**, 1068 (2019).
- [26] L. Protesescu, S. Yakunin, M. I. Bodnarchuk, F. Krieg, R. Caputo, C. H. Hendon, R. X. Yang, A. Walsh, and M. V. Kovalenko, Nanocrystals of cesium lead halide perovskites (CsPbX_3 , X = Cl, Br, and I): Novel optoelectronic materials showing bright emission with wide color Gamut, *Nano Lett.* **15**, 3692 (2015).
- [27] Q. A. Akkerman, V. D'Innocenzo, S. Accornero, A. Scarpellini, A. Petrozza, M. Prato, and L. Manna, Tuning the optical properties of cesium lead halide perovskite nanocrystals by anion exchange reactions, *J. Am. Chem. Soc.* **137**, 10276 (2015).
- [28] J. B. Hoffman, A. L. Schleper, and P. V. Kamat, Transformation of sintered CsPbBr_3 nanocrystals to cubic CsPbI_3 and

- gradient CsPbBrX_{3-x} through halide exchange, *J. Am. Chem. Soc.* **138**, 8603 (2016).
- [29] Y. Bekenstein, B. A. Koscher, S. W. Eaton, P. Yang, and A. P. Alivisatos, Highly luminescent colloidal nanoplates of perovskite cesium lead halide and their oriented assemblies, *J. Am. Chem. Soc.* **137**, 16008 (2015).
- [30] M. H. Du, Efficient carrier transport in halide perovskites: Theoretical perspectives, *J. Mater. Chem. A* **2**, 9091 (2014).
- [31] S. D. Stranks, G. E. Eperon, G. Grancini, C. Menelaou, M. J. P. Alcocer, T. Leijtens, L. M. Herz, A. Petrozza, and H. J. Snaith, Electron-hole diffusion lengths exceeding 1 micrometer in an organometal trihalide perovskite absorber, *Science* **342**, 341 (2013).
- [32] A. A. Zhumekenov, M. I. Saidaminov, M. A. Haque, E. Alarousu, S. P. Sarmah, B. Murali, I. Dursun, X. H. Miao, A. L. Abdelhady, T. Wu, O. F. Mohammed, and O. M. Bakr, Formamidinium lead halide perovskite crystals with unprecedented long carrier dynamics and diffusion length, *ACS Energy Lett.* **1**, 32 (2016).
- [33] Y. Zhao, A. M. Nardes, and K. Zhu, Solid-State mesostructured perovskite CH₃NH₃PbI₃ solar cells: Charge transport, recombination, and diffusion length, *J. Phys. Chem. Lett.* **5**, 490 (2014).
- [34] L. Protesescu, S. Yakunin, M. I. Bodnarchuk, F. Bertolotti, N. Masciocchi, A. Guagliardi, and M. V. Kovalenko, Monodisperse formamidinium lead bromide nanocrystals with bright and stable green photoluminescence, *J. Am. Chem. Soc.* **138**, 14202 (2016).
- [35] J. Kang and L. W. Wang, High defect tolerance in lead halide perovskite CsPbBr₃, *J. Phys. Chem. Lett.* **8**, 489 (2017).
- [36] H. Huang, M. I. Bodnarchuk, S. V. Kershaw, M. V. Kovalenko, and A. L. Rogach, Lead halide perovskite nanocrystals in the research spotlight: stability and defect tolerance, *ACS Energy Lett.* **2**, 2071 (2017).
- [37] R. E. Brandt, J. R. Poindexter, P. Gorai, R. C. Kurchin, R. L. Z. Hoye, L. Nienhaus, M. W. B. Wilson, J. A. Polizzotti, R. Sereika, R. Žaltauskas, L. C. Lee, J. L. Macmanus-Driscoll, M. Bawendi, V. Stevanović, and T. Buonassisi, Searching for “defect-tolerant” photovoltaic materials: Combined theoretical and experimental screening, *Chem. Mater.* **29**, 4667 (2017).
- [38] D. Meggiolaro, S. G. Motti, E. Mosconi, A. J. Barker, J. Ball, C. Andrea Riccardo Perini, F. Deschler, A. Petrozza, and F. De Angelis, Iodine chemistry determines the defect tolerance of lead-halide perovskites, *Energy Environ. Sci.* **11**, 702 (2018).
- [39] A. V. Cohen, D. A. Egger, A. M. Rappe, and L. Kronik, Breakdown of the static picture of defect energetics in halide perovskites: The case of the Br vacancy in CsPbBr₃, *J. Phys. Chem. Lett.* **10**, 4490 (2019).
- [40] D. S. Dolzhenkov, C. Wang, Y. Xu, M. G. Kanatzidis, and E. A. Weiss, Ligand-free, quantum-confined Cs₂SnI₆ perovskite nanocrystals, *Chem. Mater.* **29**, 7901 (2017).
- [41] B. W. Park, B. Philippe, X. Zhang, H. Rensmo, G. Boschloo, and E. M. J. Johansson, Bismuth based hybrid perovskites A₃Bi₂I₉ (A: methylammonium or cesium) for solar cell application, *Adv. Mater.* **27**, 6806 (2015).
- [42] J. Tilchin, D. N. Dirin, G. I. Maikov, A. Sashchiuk, M. V. Kovalenko, and E. Lifshitz, Hydrogen-like Wannier-Mott excitons in single crystal of methylammonium lead bromide perovskite, *ACS Nano* **10**, 6363 (2016).
- [43] M. Z. Mayers, L. Z. Tan, D. A. Egger, A. M. Rappe, and D. R. Reichman, How lattice and charge fluctuations control carrier dynamics in halide perovskites, *Nano Lett.* **18**, 8041 (2018).
- [44] M. Kulbak, D. Cahen, and G. Hodes, How important is the organic part of lead halide perovskite photovoltaic cells? Efficient CsPbBr₃ cells, *J. Phys. Chem. Lett.* **6**, 2452 (2015).
- [45] D. A. Egger, A. M. Rappe, and L. Kronik, Hybrid organic-inorganic perovskites on the move, *Acc. Chem. Res.* **49**, 573 (2016).
- [46] A. M. A. Leguy, J. M. Frost, A. P. McMahon, V. G. Sakai, W. Kochelmann, C. Law, X. Li, F. Foglia, A. Walsh, B. C. O’Regan, J. Nelson, J. T. Cabral, and P. R. F. Barnes, The dynamics of methylammonium ions in hybrid organic-inorganic perovskite solar cells, *Nat. Commun.* **6**, 7124 (2015).
- [47] T. Etienne, E. Mosconi, and F. De Angelis, Dynamical origin of the Rashba effect in organohalide lead perovskites: A key to suppressed carrier recombination in perovskite solar cells? *J. Phys. Chem. Lett.* **7**, 1638 (2016).
- [48] C. Roiland, G. Trippé-Allard, K. Jemli, B. Alonso, J. C. Ameline, R. Gautier, T. Bataille, L. Le Pollès, E. Deleporte, J. Even, and C. Katan, Multinuclear NMR as a tool for studying local order and dynamics in CH₃NH₃PbX₃ (X = Cl, Br, I) hybrid perovskites, *Phys. Chem. Chem. Phys.* **18**, 27133 (2016).
- [49] D. A. Egger, A. Bera, D. Cahen, G. Hodes, T. Kirchartz, L. Kronik, R. Lovrincic, A. M. Rappe, D. R. Reichman, and O. Yaffe, What remains unexplained about the properties of halide perovskites? *Adv. Mater.* **30**, 1800691 (2018).
- [50] A. D. Wright, C. Verdi, R. L. Milot, G. E. Eperon, M. A. Pérez-Osorio, H. J. Snaith, F. Giustino, M. B. Johnston, and L. M. Herz, Electron-phonon coupling in hybrid lead halide perovskites, *Nat. Commun.* **7**, 11755 (2016).
- [51] A. Mattoni, A. Filippetti, M. I. Saba, C. Caddeo, and P. Delugas, Temperature evolution of methylammonium trihalide vibrations at the atomic scale, *J. Phys. Chem. Lett.* **7**, 529 (2016).
- [52] O. Yaffe, Y. Guo, L. Z. Tan, D. A. Egger, T. Hull, C. C. Stoumpos, F. Zheng, T. F. Heinz, L. Kronik, M. G. Kanatzidis, J. S. Owen, A. M. Rappe, M. A. Pimenta, and L. E. Brus, Local Polar Fluctuations in Lead Halide Perovskite Crystals, *Phys. Rev. Lett.* **118**, 136001 (2017).
- [53] O. Yaffe, Y. Guo, T. Hull, C. C. Stoumpos, L. Z. Tan, D. A. Egger, F. Zheng, G. Szpak, O. E. Semonin, A. N. Beecher, T. F. Heinz, L. Kronik, A. M. Rappe, M. G. Kanatzidis, J. S. Owen, M. A. Pimenta, and L. E. Brus, The nature of dynamic disorder in lead halide perovskite crystals (Conference presentation), [arXiv:1604.08107](https://arxiv.org/abs/1604.08107).
- [54] D. Meggiolaro, E. Mosconi, and F. De Angelis, Formation of surface defects dominates ion migration in lead-halide perovskites, *ACS Energy Lett.* **4**, 779 (2019).
- [55] M. A. Becker, R. Vaxenburg, G. Nedelcu, P. C. Sercel, A. Shabaev, M. J. Mehl, J. G. Michopoulos, S. G. Lambrakos, N. Bernstein, J. L. Lyons, T. Stöferle, R. F. Mahrt, M. V. Kovalenko, D. J. Norris, G. Rainò, and A. L. Efros, Bright triplet excitons in caesium lead halide perovskites, *Nature (London)* **553**, 189 (2018).
- [56] V. Rinnerbauer, H. J. Egelhaaf, K. Hingerl, P. Zimmer, S. Werner, T. Warming, A. Hoffmann, M. Kovalenko, W. Heiss, G. Hesser, and F. Schaffler, Energy transfer in close-packed PbS nanocrystal films, *Phys. Rev. B* **77**, 085322 (2008).

- [57] J. Xue, R. Wang, and Y. Yang, The surface of halide perovskites from nano to bulk, *Nat. Rev. Mater.* **5**, 809 (2020).
- [58] A. J. Neukirch, W. Nie, J. C. Blancon, K. Appavoo, H. Tsai, M. Y. Sfeir, C. Katan, L. Pedesseau, J. Even, J. J. Crochet, G. Gupta, A. D. Mohite, and S. Tretiak, Polaron stabilization by cooperative lattice distortion and cation rotations in hybrid perovskite materials, *Nano Lett.* **16**, 3809 (2016).
- [59] K. Miyata, D. Meggiolaro, M. Tuan Trinh, P. P. Joshi, E. Mosconi, S. C. Jones, F. De Angelis, and X. Y. Zhu, Large polarons in lead halide perovskites, *Sci. Adv.* **3**, e1701217 (2017).
- [60] Y. Guo, O. Yaffe, T. D. Hull, J. S. Owen, D. R. Reichman, and L. E. Brus, Dynamic emission Stokes shift and liquid-like dielectric solvation of band edge carriers in lead-halide perovskites, *Nat. Commun.* **10**, 1175 (2019).
- [61] H. Zhu, K. Miyata, Y. Fu, J. Wang, P. P. Joshi, D. Niesner, K. W. Williams, S. Jin, and X.-Y. Zhu, Screening in crystalline liquids protects energetic carriers in hybrid perovskites, *Science* **353**, 1409 (2016).
- [62] M. Li, S. Bhaumik, T. W. Goh, M. S. Kumar, N. Yantara, M. Grätzel, S. Mhaisalkar, N. Mathews, and T. C. Sum, Slow cooling and highly efficient extraction of hot carriers in colloidal perovskite nanocrystals, *Nat. Commun.* **8**, 14350 (2017).
- [63] T. Ivanovska, C. Dionigi, E. Mosconi, F. De Angelis, F. Liscio, V. Morandi, and G. Ruani, Long-lived photoinduced polarons in organohalide perovskites, *J. Phys. Chem. Lett.* **8**, 3081 (2017).
- [64] T. Chen, W. L. Chen, B. J. Foley, J. Lee, J. P. C. Ruff, J. Y. P. Ko, C. M. Brown, L. W. Harriger, D. Zhang, C. Park, M. Yoon, Y. M. Chang, J. J. Choi, and S. H. Lee, Origin of long lifetime of band-edge charge carriers in organic-inorganic lead iodide perovskites, *Proc. Natl. Acad. Sci. USA* **114**, 7519 (2017).
- [65] J. M. Frost, L. D. Whalley, and A. Walsh, Slow cooling of hot polarons in halide perovskite solar cells, *ACS Energy Lett.* **2**, 2647 (2017).
- [66] H. Kawai, G. Giorgi, A. Marini, and K. Yamashita, The mechanism of slow hot-hole cooling in lead-iodide perovskite: First-principles calculation on carrier lifetime from electron-phonon interaction, *Nano Lett.* **15**, 3103 (2015).
- [67] Y. Rakita, O. Bar-Elli, E. Meirzadeh, H. Kaslasi, Y. Peleg, G. Hodes, I. Lubomirsky, D. Oron, D. Ehre, and D. Cahen, Tetragonal $\text{CH}_3\text{NH}_3\text{PbI}_3$ is ferroelectric, *Proc. Natl. Acad. Sci. USA* **114**, E5504 (2017).
- [68] Y. Rakita, E. Meirzadeh, T. Bendikov, V. Kalchenko, I. Lubomirsky, G. Hodes, D. Ehre, and D. Cahen, $\text{CH}_3\text{NH}_3\text{PbBr}_3$ is not pyroelectric, excluding ferroelectric-enhanced photovoltaic performance, *APL Mater.* **4**, 051101 (2016).
- [69] S. Liu, F. Zheng, I. Grinberg, and A. M. Rappe, Photoferroelectric and photopiezoelectric properties of organometal halide perovskites, *J. Phys. Chem. Lett.* **7**, 1460 (2016).
- [70] D. R. Ceratti, Y. Rakita, L. Cremonesi, R. Tenne, V. Kalchenko, M. Elbaum, D. Oron, M. A. C. Potenza, G. Hodes, and D. Cahen, Self-healing inside APbBr_3 halide perovskite crystals, *Adv. Mater.* **30**, 1706273 (2018).
- [71] D. Cahen and I. Lubomirsky, Self-repairing energy materials: Sine qua non for a sustainable future, *Acc. Chem. Res.* **50**, 573 (2017).
- [72] M. Isarov, L. Z. Tan, J. Tilchin, F. T. Rabouw, M. I. Bodnarchuk, R. J. A. Van Dijk-Moes, R. Carmi, Y. Barak, A. Kostadinov, I. Meir, D. Vanmaekelbergh, M. V. Kovalenko, A. M. Rappe, and E. Lifshitz, Polarized emission in II-VI and perovskite colloidal quantum dots, *J. Phys. B At. Mol. Opt. Phys.* **50**, 214001 (2017).
- [73] See Supplemental Material at <http://link.aps.org/supplemental/10.1103/PhysRevB.106.035303> for additional figures and theoretical simulation details.
- [74] K. Frohna, T. Deshpande, J. Harter, W. Peng, B. A. Barker, J. B. Neaton, S. G. Louie, O. M. Bakr, D. Hsieh, and M. Bernardi, Inversion symmetry and bulk Rashba effect in methylammonium lead iodide perovskite single crystals, *Nat. Commun.* **9**, 1829 (2018).
- [75] Y. Zhai, S. Baniya, C. Zhang, J. Li, P. Haney, C. X. Sheng, E. Ehrenfreund, and Z. V. Vardeny, Giant Rashba splitting in 2D organic-inorganic halide perovskites measured by transient spectroscopies, *Sci. Adv.* **3**, 1700704 (2017).
- [76] M. Governale, Quantum Dots with Rashba Spin-Orbit Coupling, *Phys. Rev. Lett.* **89**, 206802 (2002).
- [77] S. Hu, H. Gao, Y. Qi, Y. Tao, Y. Li, J. R. Reimers, M. Bokdam, C. Franchini, D. Di Sante, A. Stroppa, and W. Ren, Dipole order in halide perovskites: Polarization and Rashba band splittings, *J. Phys. Chem. C* **121**, 23045 (2017).
- [78] E. M. Hutter, M. C. Gélvez-Rueda, A. Osherov, V. Bulović, F. C. Grozema, S. D. Stranks, and T. J. Savenije, Direct-indirect character of the bandgap in methylammonium lead iodide perovskite, *Nat. Mater.* **16**, 115 (2017).
- [79] J. Even, L. Pedesseau, J. M. Jancu, and C. Katan, DFT and $k \cdot p$ modelling of the phase transitions of lead and tin halide perovskites for photovoltaic cells, *Phys. Status Solidi RRL* **8**, 31 (2014).
- [80] F. Brivio, K. T. Butler, A. Walsh, and M. Van Schilfgaarde, Relativistic quasiparticle self-consistent electronic structure of hybrid halide perovskite photovoltaic absorbers, *Phys. Rev. B* **89**, 155204 (2014).
- [81] A. Stroppa, D. Di Sante, P. Barone, M. Bokdam, G. Kresse, C. Franchini, M.-H. Whangbo, and S. Picozzi, Tunable ferroelectric polarization and its interplay with spin-orbit coupling in tin iodide perovskites, *Nat. Commun.* **5**, 5900 (2014).
- [82] J. Yin, P. Maity, L. Xu, A. M. El-Zohry, H. Li, O. M. Bakr, J. L. Brédas, and O. F. Mohammed, Layer-dependent Rashba band splitting in 2D hybrid perovskites, *Chem. Mater.* **30**, 8538 (2018).
- [83] H. H. Fang, J. Yang, S. Adjokatsé, E. Tekelenburg, M. E. Kamminga, H. Duim, J. Ye, G. R. Blake, J. Even, and M. A. Loi, Band-edge exciton fine structure and exciton recombination dynamics in single crystals of layered hybrid perovskites, *Adv. Funct. Mater.* **30**(6), 1907979 (2020).
- [84] J. Even, L. Pedesseau, J. M. Jancu, and C. Katan, Importance of spin-orbit coupling in hybrid organic/inorganic perovskites for photovoltaic applications, *J. Phys. Chem. Lett.* **4**, 2999 (2013).
- [85] P. C. Sercel, Z. V. Vardeny, and A. L. Efros, Circular dichroism in non-chiral metal halide perovskites, *Nanoscale* **12**, 18067 (2020).
- [86] K. Ishizaka, M. S. Bahramy, H. Murakawa, M. Sakano, T. Shimojima, T. Sonobe, K. Koizumi, S. Shin, H. Miyahara, A. Kimura, K. Miyamoto, T. Okuda, H. Namatame, M.

- Taniguchi, R. Arita, N. Nagaosa, K. Kobayashi, Y. Murakami, R. Kumai, Y. Kaneko, Y. Onose, and Y. Tokura, Giant Rashba-type spin splitting in bulk BiTeI, *Nat. Mater.* **10**, 521 (2011).
- [87] G. Bihlmayer, S. Blügel, and E. V. Chulkov, Enhanced Rashba spin-orbit splitting in BiAg (111) and PbAg (111) surface alloys from first principles, *Phys. Rev. B* **75**, 195414 (2007).
- [88] M. Fu, P. Tamarat, H. Huang, J. Even, A. L. Rogach, and B. Lounis, Neutral and charged exciton fine structure in single lead halide perovskite nanocrystals revealed by magneto-optical spectroscopy, *Nano Lett.* **17**, 2895 (2017).
- [89] M. Kim, J. Im, A. J. Freeman, J. Ihm, and H. Jin, Switchable $s = 1/2$ and $j = 1/2$ Rashba bands in ferroelectric halide perovskites, *Proc. Natl. Acad. Sci. USA* **111**, 6900 (2014).
- [90] A. Amat, E. Mosconi, E. Ronca, C. Quarti, P. Umari, M. K. Nazeeruddin, M. Grätzel, and F. De Angelis, Cation-induced band-gap tuning in organohalide perovskites: Interplay of spin-orbit coupling and octahedra tilting, *Nano Lett.* **14**, 3608 (2014).
- [91] A. Marronnier, G. Roma, M. A. Carignano, Y. Bonnassieux, C. Katan, J. Even, E. Mosconi, and F. De Angelis, Influence of disorder and anharmonic fluctuations on the dynamical Rashba effect in purely inorganic lead-halide perovskites, *J. Phys. Chem. C* **123**, 291 (2019).
- [92] G. Rainò, G. Nedelcu, L. Protesescu, M. I. Bodnarchuk, M. V. Kovalenko, R. F. Mahrt, and T. Stöferle, Single cesium lead halide perovskite nanocrystals at low temperature: Fast single-photon emission, Reduced blinking, and exciton fine structure, *ACS Nano* **10**, 2485 (2016).
- [93] J. A. Steele, P. Puech, B. Monserrat, B. Wu, R. X. Yang, T. Kirchartz, H. Yuan, G. Fleury, D. Giovanni, E. Fron, M. Keshavarz, E. Debroye, G. Zhou, T. C. Sum, A. Walsh, J. Hofkens, and M. B. J. Roelofs, Role of electron-phonon coupling in the thermal evolution of bulk Rashba-like spin-split lead halide perovskites exhibiting dual-band photoluminescence, *ACS Energy Lett.* **4**, 2205 (2019).
- [94] T. Wang, B. Daiber, J. M. Frost, S. A. Mann, E. C. Garnett, A. Walsh, and B. Ehrler, Indirect to direct bandgap transition in methylammonium lead halide perovskite, *Energy Environ. Sci.* **10**, 509 (2017).
- [95] M. J. Crane, L. M. Jacoby, T. A. Cohen, Y. Huang, C. K. Luscombe, and D. R. Gamelin, Coherent spin precession and lifetime-limited spin dephasing in CsPbBr₃ perovskite nanocrystals, *Nano Lett.* **20**, 8626 (2020).
- [96] M. Aebli, L. Piveteau, O. Nazarenko, B. M. Benin, F. Krieg, R. Verel, and M. V. Kovalenko, Lead-Halide scalar couplings in 207Pb NMR of APbX₃ perovskites (A = Cs, methylammonium, formamidinium; X = Cl, Br, I), *Sci. Rep.* **10**, 8229 (2020).
- [97] Z. G. Yu, Effective-mass model and magneto-optical properties in hybrid perovskites, *Sci. Rep.* **6**, 28576 (2016).
- [98] X. Zhang, J. X. Shen, and C. G. Van De Walle, Three-dimensional spin texture in hybrid perovskites and its impact on optical transitions, *J. Phys. Chem. Lett.* **9**, 2903 (2018).
- [99] R. Wang, S. Hu, X. Yang, X. Yan, H. Li, and C. Sheng, Circularly polarized photoluminescence and Hanle effect measurements of spin relaxation in organic-inorganic hybrid perovskite films, *J. Mater. Chem. C* **6**, 2989 (2018).
- [100] J. Ramade, L. M. Andriambarijaona, V. Steinmetz, N. Goubet, L. Legrand, T. Barisien, F. Bernardot, C. Testelin, E. Lhuillier, A. Bramati, and M. Chamarro, Fine structure of excitons and electron-hole exchange energy in polymorphic CsPbBr₃ single nanocrystals, *Nanoscale* **10**, 6393 (2018).
- [101] V. L. Berkovits, C. Hermann, G. Lampel, A. Nakamura, and V. I. Safarov, Giant Overhauser shift of conduction-electron spin resonance due to optical polarization of nuclei in semiconductors, *Phys. Rev. B* **18**, 1767 (1978).
- [102] B. Eble, O. Krebs, A. Lemaître, K. Kowalik, A. Kudelski, P. Voisin, B. Urbaszek, X. Marie, and T. Amand, Dynamic nuclear polarization of a single charge-tunable InAs GaAs quantum dot, *Phys. Rev. B* **74**, 081306(R) (2006).
- [103] P. L. Kuhns, A. Kleinhammes, T. Schmiedel, W. G. Moulton, P. Chabrier, S. Sloan, E. Hughes, and C. R. Bowers, Magnetic-field dependence of the optical Overhauser effect in GaAs, *Phys. Rev. B* **55**, 7824 (1997).
- [104] S. Koizumi, Mitsuo, Goto, Jun, and Matsuki, Dynamic nuclear self-polarization of III-V semiconductors, *J. Semicond.* **39**, 082001 (2018).
- [105] H. A. Tetsu Ito, S. W., Masao Ichida, Hideki Gotoh, and Hidehiko Kamada, Overhauser effect and anisotropy of electron spin g-factor in GaAs/AlGaAs quantum wells, *J. Autom. Mob. Robot. Intell. Syst.* **3**, 105 (2009).
- [106] C. Le Gall, A. Brunetti, H. Boukari, and L. Besombes, Electron-Nuclei spin dynamics in II-VI semiconductor quantum dots, *Phys. Rev. B* **85**, 195312 (2012).
- [107] I. A. Merkulov, A. L. Efros, and M. Rosen, Electron spin relaxation by nuclei in semiconductor quantum dots, *Phys. Rev. B* **65**, 205309 (2002).
- [108] E. Lifshitz, L. Fradkin, A. Glozman, and L. Langof, Optically detected magnetic resonance studies of colloidal semiconductor nanocrystals, *Annu. Rev. Phys. Chem.* **55**, 509 (2004).
- [109] R. Strassberg, S. Delikanli, Y. Barak, J. Dehnel, A. Kostadinov, G. Maikov, P. L. Hernandez-Martinez, M. Sharma, H. V. Demir, and E. Lifshitz, Persuasive evidence for electron-nuclear coupling in diluted magnetic colloidal nanoplatelets using optically detected magnetic resonance spectroscopy, *J. Phys. Chem. Lett.* **10**, 4437 (2019).
- [110] C. M. Iaru, J. J. Geuchies, P. M. Koenraad, D. Vanmaekelbergh, and A. Y. Silov, Strong carrier-phonon coupling in lead halide perovskite nanocrystals, *ACS Nano* **11**, 11024 (2017).
- [111] K. E. Knowles, H. D. Nelson, T. B. Kilburn, and D. R. Gamelin, Singlet-Triplet splittings in the luminescent excited states of colloidal Cu⁺:CdSe, Cu⁺:InP, and CuInS₂ nanocrystals: Charge-transfer configurations and self-trapped excitons, *J. Am. Chem. Soc.* **137**, 13138 (2015).
- [112] S. Li, J. Luo, J. Liu, and J. Tang, Self-trapped excitons in all-inorganic halide perovskites: Fundamentals, status, and potential applications, *J. Phys. Chem. Lett.* **10**, 1999 (2019).
- [113] K. M. McCall, C. C. Stoumpos, S. S. Kostina, M. G. Kanatzidis, and B. W. Wessels, Strong electron-phonon coupling and self-trapped excitons in the defect halide perovskites A₃M₂I₉ (A = Cs, Rb; m = Bi, Sb), *Chem. Mater.* **29**, 4129 (2017).
- [114] A. Buin, R. Comin, J. Xu, A. H. Ip, and E. H. Sargent, Halide-dependent electronic structure of organolead perovskite materials, *Chem. Mater.* **27**, 4405 (2015).

- [115] P. Tamarat, L. Hou, J. B. Trebbia, A. Swarnkar, L. Biadala, Y. Louyer, M. I. Bodnarchuk, M. V. Kovalenko, J. Even, and B. Lounis, The dark exciton ground state promotes photon-pair emission in individual perovskite nanocrystals, *Nat. Commun.* **11**, 6001 (2020).
- [116] M. A. Becker, C. Bernasconi, M. I. Bodnarchuk, G. Raino, M. V. Kovalenko, D. J. Norris, R. F. Mahrt, and T. Stoferle, Unraveling the origin of the long fluorescence decay component of cesium lead halide perovskite nanocrystals, *ACS Nano* **14**, 14939 (2020).
- [117] E. V. Shornikova, D. R. Yakovlev, L. Biadala, S. A. Crooker, V. V. Belykh, M. V. Kochiev, A. Kuntzmann, M. Nasilowski, B. Dubertret, and M. Bayer, Negatively charged excitons in CdSe nanoplatelets, *Nano Lett.* **20**, 1370 (2020).
- [118] P. C. Sercel, J. L. Lyons, D. Wickramaratne, R. Vaxenburg, N. Bernstein, and A. L. Efros, Exciton fine structure in perovskite nanocrystals, *Nano Lett.* **19**, 4068 (2019).
- [119] C. Zhang, D. Sun, Z. G. Yu, C. X. Sheng, S. McGill, D. Semenov, and Z. V. Vardeny, Field-Induced spin splitting and anomalous photoluminescence circular polarization in $\text{CH}_3\text{NH}_3\text{PbI}_3$ films at high magnetic field, *Phys. Rev. B* **97**, 134412 (2018).
- [120] F. Meier and B. P. Zakharchenya, *Optical Orientation* (Elsevier, New York, 2012).